Original article

# Investigation of microstructural and magnetic properties of Ca$^{2+}$ doped strontium hexaferrite nanoparticles

Sachin Kumar Godara [a], Mankamal Preet Kaur [a], Varinder Kaur [a], Parambir Singh Malhi [a], Mandeep Singh [b], Swati Verma [b], Rohit Jasrotia [c], Jahangeer Ahmed [d,*], Mohaseen S. Tamboli [e], Ashwani Kumar Sood [a,*]

[a] Department of Chemistry, UGC Centre for Advanced Studies-II, Guru Nanak Dev University, Amritsar, Punjab 143005, India
[b] Department of Physics, Guru Nanak Dev University, Amritsar, Punjab 143005, India
[c] School of Physics and Materials Science, Shoolini University of Biotechnology and Management, Bajhol, Solan, Himachal Pradesh, India
[d] Department of Chemistry, College of Science, King Saud University, P.O. Box 2455, Riyadh 11451, Saudi Arabia
[e] School of Chemical Engineering, Yeungnam University, Gyeongsan 38541, Republic of Korea

## ARTICLE INFO

## ABSTRACT

The effect of Ca$^{2+}$ ions doping on the structure, magnetic properties, and surface morphology of Sr$_{1-x}$Ca$_x$Fe$_{12}$O$_{19}$ (x = 0.0 to 0.5 with step size 0.1) hexaferrite nanoparticles synthesized using the sol–gel auto-combustion technique was investigated in the current study. The phase purity of synthesized samples is confirmed by XRD data plots up to x = 0.2, after which $\alpha$-Fe$_2$O$_3$ was observed as a secondary phase in all concentrations. The micrographs from FESEM show that with the increase in the concentration of Ca$^{2+}$ dopant, the average grain size increases from $\approx$125 nm to $\approx$240 nm. The intensity of secondary phase Raman peaks increases with increasing dopant ion concentration beyond x = 0.2. The coercivity value varies between 5292 and 5828 Oe as the Ca$^{2+}$ dopant increases. A maximum (72.63 emu/g) value of saturation magnetization ($M_s$) have been obtained in samples at x = 0.2. Such substances can be utilized for making permanent magnets applications.

© 2022 The Author(s). Published by Elsevier B.V. on behalf of King Saud University. This is an open access article under the CC BY-NC-ND license (http://creativecommons.org/licenses/by-nc-nd/4.0/).

## 1. Introduction

In the field of ferrite-based permanent magnetic materials, the discovery of M-type (Magnetoplumbite) hexaferrite in the 1950s marked a watershed moment (Pullar 2012). Due to their critical role in the fabrication of key components for many different devices and machines, magnetic materials are in high demand in the electronics industry. High coercivity, high magnetic saturation and remanence, high magnetocrystalline anisotropy, excellent chemical stability, and a high Curie temperature have all been associated with M-type hexaferrite (Urbano-Peña et al., 2019). A search for low-cost (Mehtab et al., 2022; Ahmad et al., 2013) and

high-performance magnetic material leads to the development of new M-type hexaferrite material. Ca is available in abundance in our earth bulk as compared to their Ba and Sr and hence its metal nitrate and oxides are cheaper than other counterparts Ba (Christy et al., 2019). If calcium hexaferrite (CaM) could be synthesized in phase pure form, it would be a low-cost substitute for Ba/Sr - based hexaferrite. Hexaferrites contain one large divalent metal ion (M$^{2+}$=Ba/Sr/Pb/Ca), which disrupts the crystal lattice due to size differences, resulting in high magnetocrystalline anisotropy. Lotgering (Lotgering and Huyberts 1980) described lanthanum ferrite as a material with large magnetocrystalline anisotropy. Ca is least studied as a dopant in M-type hexaferrites. Ca-doped hexaferrites have been shown to improve coercivity, increase the reaction rate, lower phase formation temperature, and thus control grain size more easily (Chauhan et al., 2018; Sable et al., 2010; Ali et al., 2013). As a result, it is worthwhile to investigate the magnetic properties of MFe$_{12}$O$_{19}$ by replacing M$^{2+}$ with Ca$^{2+}$. The current study reports on the synthesis of Sr$_{1-x}$Ca$_x$Fe$_{12}$O$_{19}$ (x = 0.0 to 0.5) hexaferrite nanoparticles over a wide concentration range. The magnetic, morphological, and structural characteristics of the prepared samples were studied in depth.

* Corresponding authors.
   E-mail addresses: jahmed@ksu.edu.sa (J. Ahmed), aksoodchem@yahoo.co.in (A.K. Sood).

Peer review under responsibility of King Saud University.

**Production and hosting by Elsevier**

## 2. Experimental

To synthesize $Ca^{2+}$-doped strontium hexaferrite nanoparticles (by sol–gel auto-combustion method), calcium nitrate, ferric nitrate, strontium nitrate, and citric acid (all the chemicals were AR grade having purity >98%) were used as such without further purification. Double distilled water was used to dissolve metal nitrate salts in the required stoichiometric ratio (as listed in Table 1). Afterward, the citric acid was mixed in the above solution on a magnetic stirrer at room temperature. Ammonia solution (25%) was added drop-wise to maintain a pH of 7. The temperature of the resulting solution was raised to 90–100 °C using a hot plate. With continuous heating for a few hours, the excess water evaporates, leaving a brown gel that looks like honey. The gel was kept in an oven for 1 h at 200 °C to allow auto combustion reactions. Mixed metal oxide precursor material was obtained after the auto-combustion reaction. Impurities were removed from the powder samples using a muffle furnace and calcination for 6 h at 900 °C to convert the amorphous phase to the crystalline phase.

The Rigaku Miniflex-II diffractometer (20-80° range of 2θ utilizing Cu-α emission ($\lambda$ = 1.54 A), 0.005 step size) was used to study the phase purity, and structure of the materials. FESEM (operating voltage 20 kV) from JEOL, JSM-7100, and energy dispersive X-ray (EDX) analysis were carried out for surface morphology and elemental analysis. Confocal Renishaw Raman Spectrophotometer having laser of 514 nm excitation wavelength was used to obtain structural features in 100–800 $cm^{-1}$ wavenumber range. VSM (vibrating sample magnetometer, Microsense EV-90) was used to make magnetic measurements.

## 3. Results and discussion

XRD data of the $Sr_{(1-x)}Ca_xFe_{12}O_{19}$ (x = 0.0–0.5) materials is shown in Fig. 1. According to international standard diffraction data, the peaks of all six compositions correspond to the M-type strontium hexaferrite phase (Godara et al., 2022). At concentration x $\geq$ 0.3, additional peaks marked with '*', indicating hematite (α-$Fe_2O_3$) secondary phase was observed. The intensity of the $\langle 107 \rangle$ and $\langle 114 \rangle$ planes decreases as dopant ion concentration increases, while the intensity of the α-$Fe_2O_3$ peak increases. As a result, as the concentration of $Ca^{2+}$ doping increases, the α-$Fe_2O_3$ phase grows at the expense of the M-type phase. This indicates lower calcium solubility in SrM phase at 900 °C. The lower solubility of calcium is due to its smaller ionic radii, which is responsible for the appearance of the hematite phase. The calcium solubility can be improved by increasing calcination temperature and time (Mohammed et al., 2018; Ahmad et al., 2013).

Rietveld refinement was performed by Fullprof software to further establish %age phase purity and determine other structural characteristics. For Rietveld refinement, the basic structure (starting lattice parameters and atomic locations) was assumed the same as in ISCD 98-002-6353. The procedure is also reported elsewhere (Godara et al., 2019). The corrected data matches the
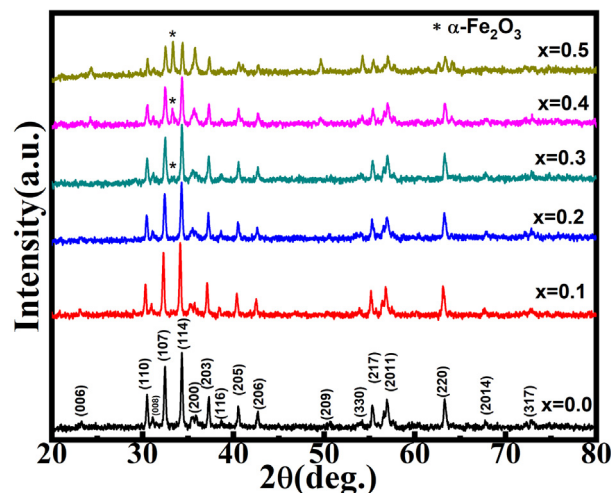


**Fig. 1.** XRD patterns for $Sr_{(1-x)}Ca_xFe_{12}O_{19}$ (x = 0.0–0.5).

experimental data fairly well, and the difference data is randomly distributed around zero, as seen in Fig. 2. The Rietveld refined parameters for x = 0.0–0.5 were tabulated in Table 2.

The lattice constants 'c & a' as well as cell volume decreases with an increase 'x = 0.2,' while the lattice constants 'a & c' as well as cell volume randomly varies for x > 0.2 due to the appearance of the hematite phase. The observed decrease in cell volume and the lattice constants 'a & c' could be due to the smaller ionic radius of $Ca^{2+}$ (0.99) (Ubaidullah et al., 2020) compared to $Sr^{2+}$ ((1.49) Kaur et al., 2017). As a result of the decrease in lattice parameters, it can be concluded that the incorporation of $Ca^{2+}$ ions into the crystal structure of $SrFe_{12}O_{19}$ was successful. Verstegen and Stevels have already demonstrated that if the observed c/a ratio is less than 3.98 (Yang et al., 2014), the structure is assumed to be M-type. The observed c/a values in all synthesized samples are less than **3.93**, confirming the M-type hexaferrite phase. The presence of secondary phases, bond length, local and dynamic symmetry, local strain, and structural distortion of M-type hexaferrite materials can be investigated using Raman spectroscopy. The Raman spectra of $Sr_{(1-x)}Ca_xFe_{12}O_{19}$ (x = 0.0–0.5) are shown in Fig. 3. When compared to the literature (Kaur et al., 2017; Ashima et al., 2012; Alhokbany et al.,2021), our results show that x $\geq$ 0.3, has two more peaks of α-$Fe_2O_3$ secondary phase at 224 and 290 $cm^{-1}$, in addition to peaks corresponding to SrM phase at 85, 183, 314, 337, 411, 527, 615 and 684 $cm^{-1}$.

XRD data also exhibits α-$Fe_2O_3$ secondary phase for x $\geq$ 0.3, suggesting the existence of secondary phase which agrees well with the results obtained from Raman spectroscopy. The sharpness and the intensity of the secondary phase (α-Fe2O3) peaks increase beyond x = 0.2, which reveals that the concentration of α-$Fe_2O_3$ continuously increases with calcium doping. Due to $E_{1g}$ symmetry,

**Table 1**
Various chemicals used for synthesizing $Sr_{(1-x)}Ca_xFe_{12}O_{19}$ samples.

| Composiiton | Strontium nitrate (g) | Calcium nitrate (g) | Ferric nitrate (g) | Citric acid (g) |
|---|---|---|---|---|
| $SrFe_{12}O_{19}$ | 2.116 | 0 | 48.48 | 25 |
| $Sr_{0.9}Ca_{0.1}Fe_{12}O_{19}$ | 1.904 | 0.236 | 48.48 | 25 |
| $Sr_{0.8}Ca_{0.2}Fe_{12}O_{19}$ | 1.693 | 0.473 | 48.48 | 25 |
| $Sr_{0.7}Ca_{0.3}Fe_{12}O_{19}$ | 1.480 | 0.708 | 48.48 | 25 |
| $Sr_{0.6}Ca_{0.4}Fe_{12}O_{19}$ | 1.269 | 0.945 | 48.48 | 25 |
| $Sr_{0.5}Ca_{0.5}Fe_{12}O_{19}$ | 1.058 | 1.180 | 48.48 | 25 |
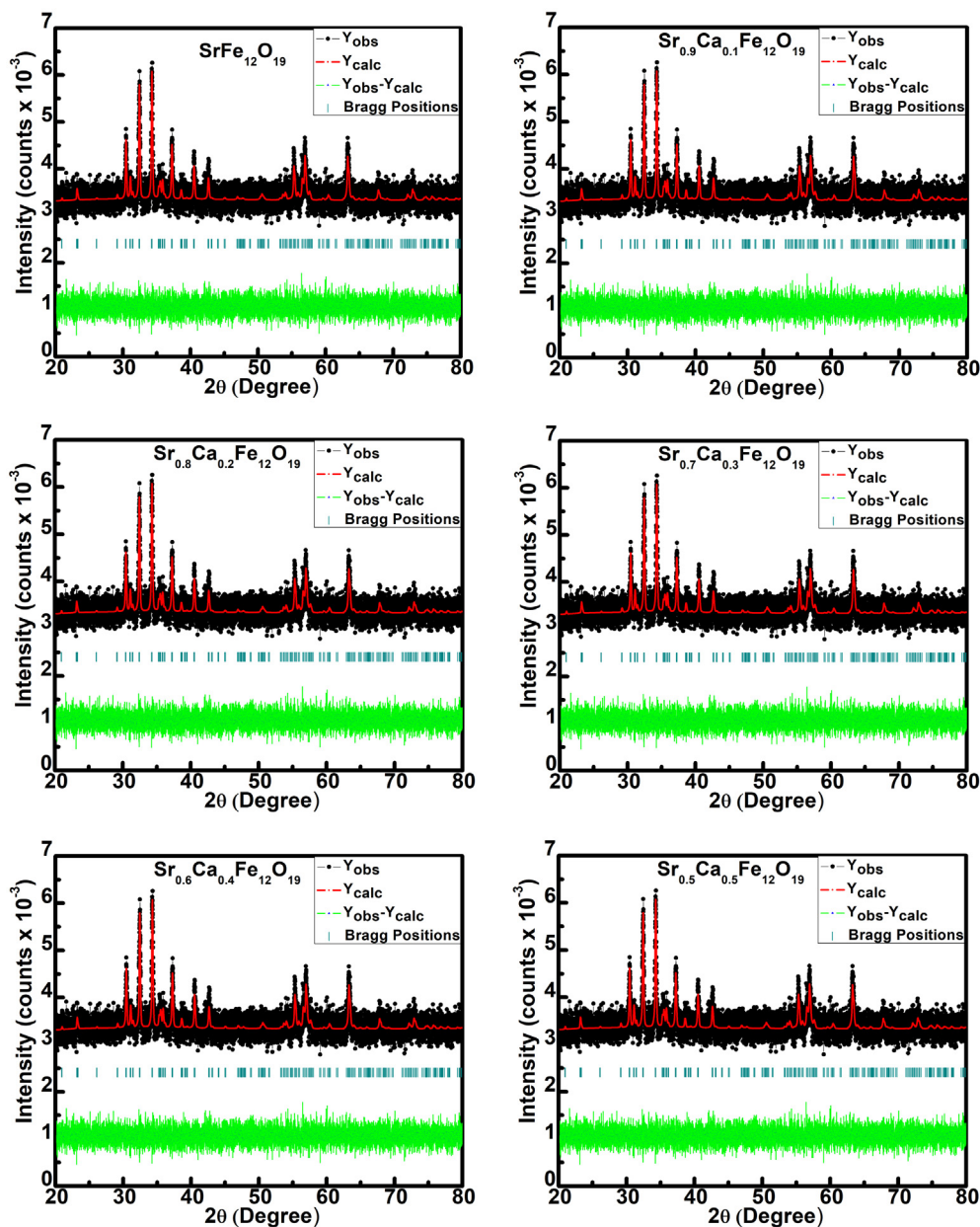
**Fig. 2.** Rietveld refinement of $Sr_{1-x}Ca_xFe_{12}O_{19}$ (x = 0.0–0.5).

**Table 2**
Rietveld refined structural parameters for $Sr_{(1-x)}Ca_xFe_{12}O_{19}$ (x = 0.0–0.5) samples.

| Composition (x) | c (Å) | a = b (Å) | V (Å)$^3$ | c/a | GoF | M-type Phase %age | Hematite phase %age |
|---|---|---|---|---|---|---|---|
| 0.0 | 23.0383 | 5.8759 | 689.3153 | 3.920812 | 7.07 | 100 | absent |
| 0.1 | 23.0206 | 5.8751 | 688.5981 | 3.918333 | 6.99 | 100 | absent |
| 0.2 | 22.2972 | 5.8689 | 665.5527 | 3.799213 | 7.13 | 100 | absent |
| 0.3 | 23.0270 | 5.8757 | 688.9303 | 3.919022 | 7.11 | 97.64 | 2.36 |
| 0.4 | 23.0193 | 5.8760 | 688.7702 | 3.917512 | 6.80 | 84.01 | 15.99 |
| 0.5 | 23.0463 | 5.8756 | 689.4842 | 3.922374 | 6.77 | 68.91 | 31.09 |

the mode at 183 matching to the vibrational mode of the entire spinel block were discovered at lower Raman shift (Mohammed et al., 2020, Musa et al., 2021). The vibrational mode observed around 314 and 337 $cm^{-1}$ occurs due to the O-Fe-O vibrations. The mode around 411 $cm^{-1}$ transpires may be due to the Fe (12 k)/Ca(12 k)$O_6$ octahedra vibrations whereas, the mode around
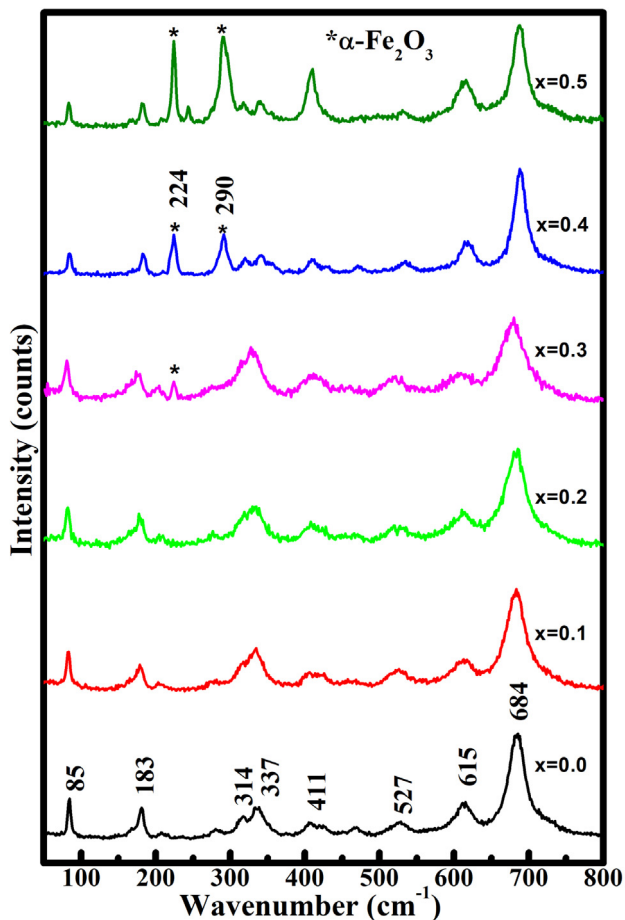
**Fig. 3.** Raman spectra for $Sr_{(1-x)}Ca_xFe_{12}O_{19}$ (x = 0.0–0.5).

527 cm$^{-1}$ arises due to the Fe(4f$_2$)/Ca(4f$_2$)O$_6$ octahedra vibrations. In addition, the Raman active modes around 615 cm$^{-1}$ and 684 cm$^{-1}$ may be occurred due to the vibrations of anion sublattices called as, Fe(2b)/Ca(2b)O$_5$ and Fe(4f$_1$)/Ca(4f$_1$)O$_4$ respectively (Jasrotia et al., 2020).

FESEM micrographs of $Sr_{(1-x)}Ca_xFe_{12}O_{19}$ (x = 0.0, 0.1,0.3,0.5) are shown in Fig. 4. In FESEM micrographs, particles are highly agglomerated (as a result of magnetic interaction between the individual grains of the samples) [Trudel et al., 2019] and the average particle size continuously increases from 125 nm (x = 0.0) to 240 nm (x = 0.5). Godara et al. also reported similar trends in literature at higher calcination temperature 1200 °C (Godara et al., 2021, Mohammed et al., 2018, Mohammed et al., 2019). The grain size increases upon replacing $Sr^{2+}$ ion with a smaller radius of $Ca^{2+}$ ion in samples from x = 0.0 to 0.5. The smaller size of $Ca^{2+}$ ion facilitates ionic diffusion and thus promotes the growth of grains (Godara et al., 2021; Blanco and Gonzalez, 1989). The small spherical-shaped particles on the surface of agglomerated grains in the significant number were observed only in the x = 0.5 sample, which may be secondary hematite phase present in a considerable amount as also revealed in XRD plots. The elemental data for samples (x = 0.1, 0.3, and 0.5) are tabulated in the inset of EDX spectra in Fig. 5. The EDX spectra show the presence of Ca, Sr, Fe and O atoms. The observed increase in Ca content confirms the successful replacement of Strontium ions by calcium ions in prepared samples.

The M-H plots were recorded at room temperature in pellet form for $Sr_{(1-x)}Ca_xFe_{12}O_{19}$ (x = 0.0–0.50) is shown in Fig. 6a and 6b. M-H plots revealed the non-saturating behavior of all the synthesized samples in the applied field range. To obtain M$_s$, saturation law i.e plotting M vs. 1/H$^2$ data, and then a straight line was fitted to it, which was then used in data of M vs. H in the range 8 to 18 kOe (Godara et al., 2021) using equation (3). The fitting plot of a straight line is shown in Fig. 6c.

$$M = M_S\left(1 - \frac{A}{H} - \frac{B}{H^2}\right) + \chi_P H \qquad (3)$$

Here M$_s$ stands for saturation magnetization, A stands for inhomogeneity, $\chi_P$ stands for high field susceptibility, and B stands for anisotropy. A linear relationship between M and 1/H$^2$ from 8 to 18 kOe was observed. As a result, the A/H and $\chi_P$ terms in Eq. (3) can be ignored. The magnetic parameters derived from M vs. H graphs are provided in Table 3 for all the studied samples. The M$_s$ value increases from 67.87 for x = 0.0 sample to 72.38 emu/g (theoretical limit of pure SrM is 72 emu/g (Shirk and Buessem, 1970) for x = 0.20 sample afterward decrease with a calcium content (due to the formation antiferromagnetic secondary phase ($\alpha$-Fe$_2$O$_3$) beyond x = 0.2). The increase M$_s$ can be discussed as follows: (a) With the increase in dopant Ca$^{2+}$ concentration upto x = 0.20 (Hooda et al., 2015), the particle size increases. This is because larger particles have a more extensive domain size and therefore align many atomic spins in a fixed direction.

The overall magnetic moment increases due the alignment of atomic spins in a particular direction when the magnetic field is applied. (b) At a lower substitution level, some of the Fe$^{3+}$ sites and Sr$^{2+}$ sites are occupied by Ca$^{2+}$ ions because of their relatively small ionic radius at 4f$_2$ spin down and 2a spin-up position (Hooda et al., 2015). When the substitution level is higher, as communicated earlier (Godara et al., 2021) 12 k up spin site and 4f$_2$ down spin sites are also occupied by Ca$^{2+}$ ions. Ca$^{2+}$ ions successfully substituted upto x = 0.20 without forming any secondary phase, therefore, these ions are expected to occupy a significant part of the down spin sites. It results in the fall in the oppositely oriented Fe$^{3+}$ (down spin) ions concentration, consequently an increase in the values of M$_s$. Conversely to our observation of M$_s$. A continuous decrease in M$_s$ values in $Sr_{1-x}Ca_xFe_{11.5}Co_{0.5}O_{19}$ (x = 0.10–0.50) samples have been reported by Ali et al. (Ali et al., 2013). Whereas H$_c$ values increased to x = 0.20 and then decreased afterward. Other researchers working in M-type hexaferrite groups have also been reported a similar trend (Hooda et al., 2015; Yuping et al., 2018; Kumar et al., 2018). The variation of M$_s$, M$_r$, H$_c$ and H$_a$ as a function of 'x' for $Sr_{1-x}Ca_xFeO_{19}$ (x = 0.0–0.5) is shown in Fig. 6d.

Furthermore, for crystals with hexagonal symmetry, B can be written as:.

$$B = \frac{H_a^2}{15} = \frac{4K_1^2}{15M_S^2} \qquad (4)$$

H$_a$ and K$_1$ represent to anisotropy field, and anisotropy constant respectively. The value of B can be calculated by plotting M = M$_s$(1-B/H$^2$) against 1/H$^2$. Furthermore, the anisotropy field, H$_a$, can be calculated by plugging the value of B into Eq. (4) (Singh et al., 2008). The coercivity (H$_c$) value is decreased from 5788 to 5292 Oe with an increase in x from 0.0 to 0.3 increases afterward till x = 0.5. It's linked to (a) a decrease in the anisotropy field (H$_a$) (Iqbal et al., 2009; Abdellah et al., 2018), (b) oxygen vacancies that act as domain wall pinning centers (Kumar et al., 2015), (c) presence of secondary phases and (d) Ca dopant-induced grain growth [Godara et al., 2021]. The presence of Fe$^{3+}$ on sites of hexagonal unit cells contributing to H$_a$ with a trend of 12 k < 4f1 < 2a < 4f2 < 2b (Li et al., 2000; Singh et al., 2008) causes
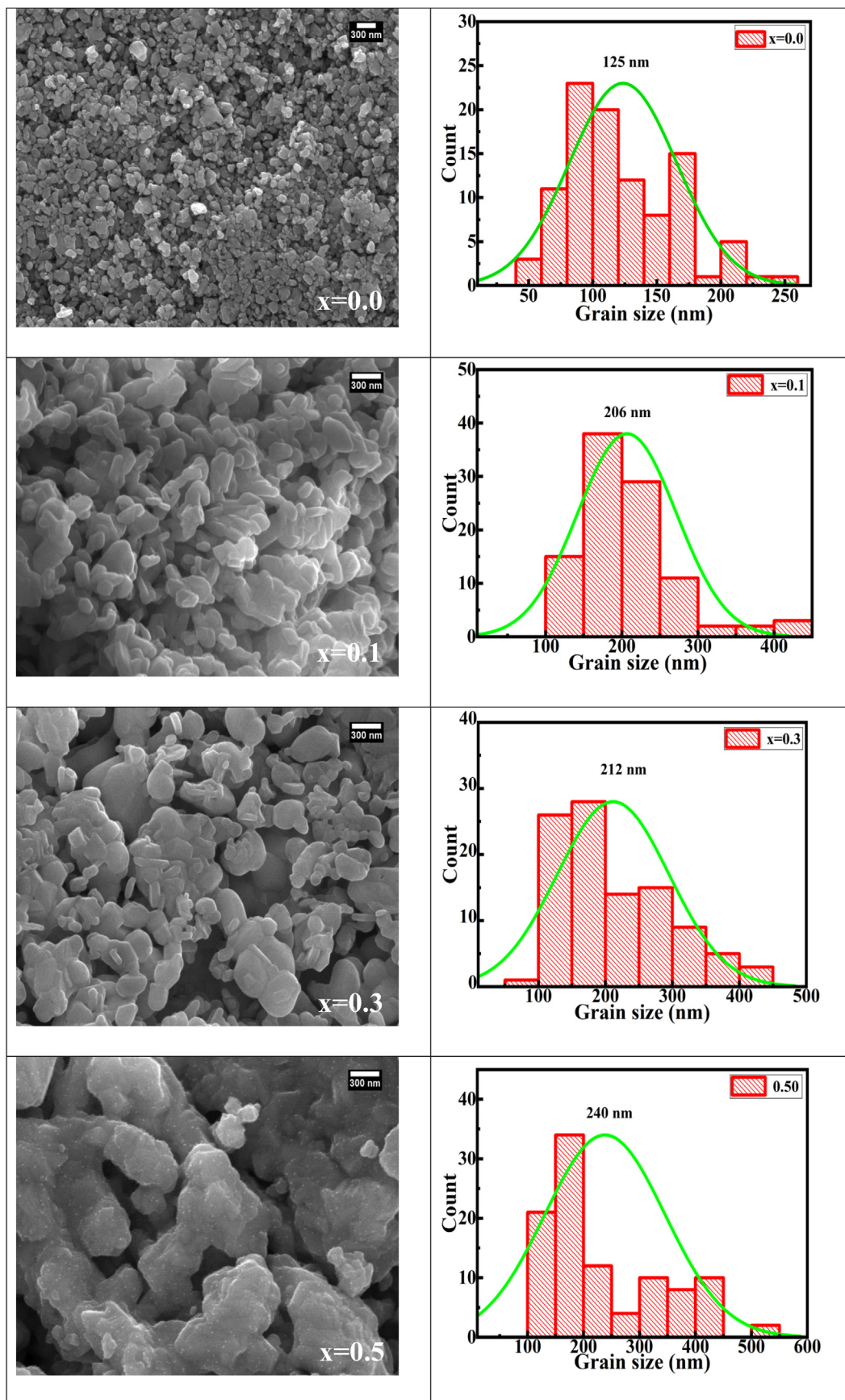
**Fig. 4.** FESEM micrographs and histograms for $Sr_{(1-x)}Ca_xFe_{12}O_{19}$ (x = 0.0, 0.1, 0.3, and 0.5).
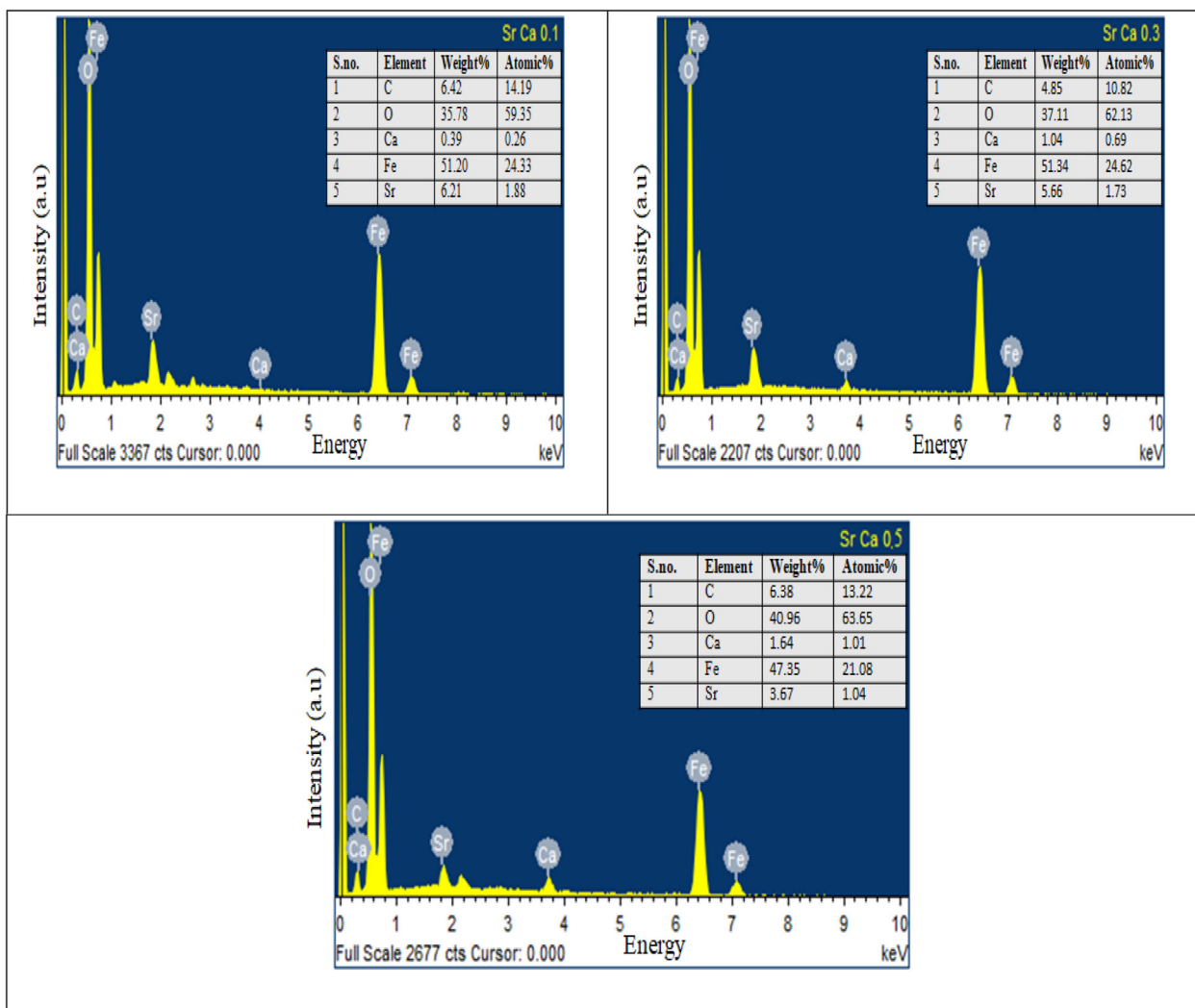
**Fig. 5.** EDX spectra of $Sr_{(1-x)}Ca_xFe_{12}O_{19}$ (x = 0.1, 0.3, and 0.5).

a decrease in $H_a$, and different authors have reported significant contributions. From x = 0.0 (18.87 kOe) to 0.3 (17.23 kOe), there is a $\approx 8$ percent drop in the anisotropy field ($H_a$) as shown in Table 3. On the other hand, doping results in a significant increase in grain size (from 125 (x = 0.0) to 240 nm (x = 0.5)), as shown in Fig. 3. Coercivity has an inverse relationship with grain size (above critical grain size). In the present study, It has been observed that both grain size and anisotropy field ($H_a$) contribute towards the reduction of coercivity with an increased dopant ion concentration upto x = 0.30. However, the anisotropy field has a greater influence on the mechanism of coercivity than grain from x = 0.0 to x = 0.5. Single domains, highly anisotropic, and magnetically hard materials have a squareness ratio greater than 0.5. However, the material is multi-domain and randomly oriented in nature if the squareness ratio is less than 0.50. Therefore, a high squareness ratio is beneficial to permanent magnets and magnetic recording (Habanjar et al., 2020). The value of squareness ratio is $\approx 0.5$ in all the synthesized samples suggesting that the hexaferrite obtained are randomly oriented single domain particles (Chauhan et al., 2018).

## 4. Conclusion

$Sr_{1-x}Ca_xFe_{12}O_{19}$ (x = 0.0–0.5) materials were synthesized from the sol–gel auto-combustion method. Phase purity in $Sr_{1-x}Ca_xFe_{12}O_{19}$ samples upto x = 0.20 is confirmed by XRD data beyond which $\alpha$–$Fe_2O_3$ secondary phase is observed. FESEM indicates that grain size monotonically increases with an increase in $Ca^{2+}$ content. The enhanced grain size as the amount of Ca doping increases is because Ca acts as a grain growth promoter. Non-linear M vs. H loops show the existence of strong magnetic ordering in all the samples. The enhancement in $M_s$ from 67.87 emu/g with x = 0.0 to 72.63 emu/g with x = 0.2 is the replacement of non-magnetic $Ca^{2+}$ in place of $Fe^{3+}$ ions at spin down (4f$_2$) sites along with $Sr^{2+}$ site and increase in domain size with grain growth. The reduction in coercivity from 5799 Oe (at x = 0.00) to 5292 Oe (x = 0.30) has been related to the corresponding decrease in $H_a$. The large values of $M_s$ (72.63 emu/g) and $H_c$ (5388 Oe) in the x = 0.20 sample are useful for low-cost permanent magnet devices.
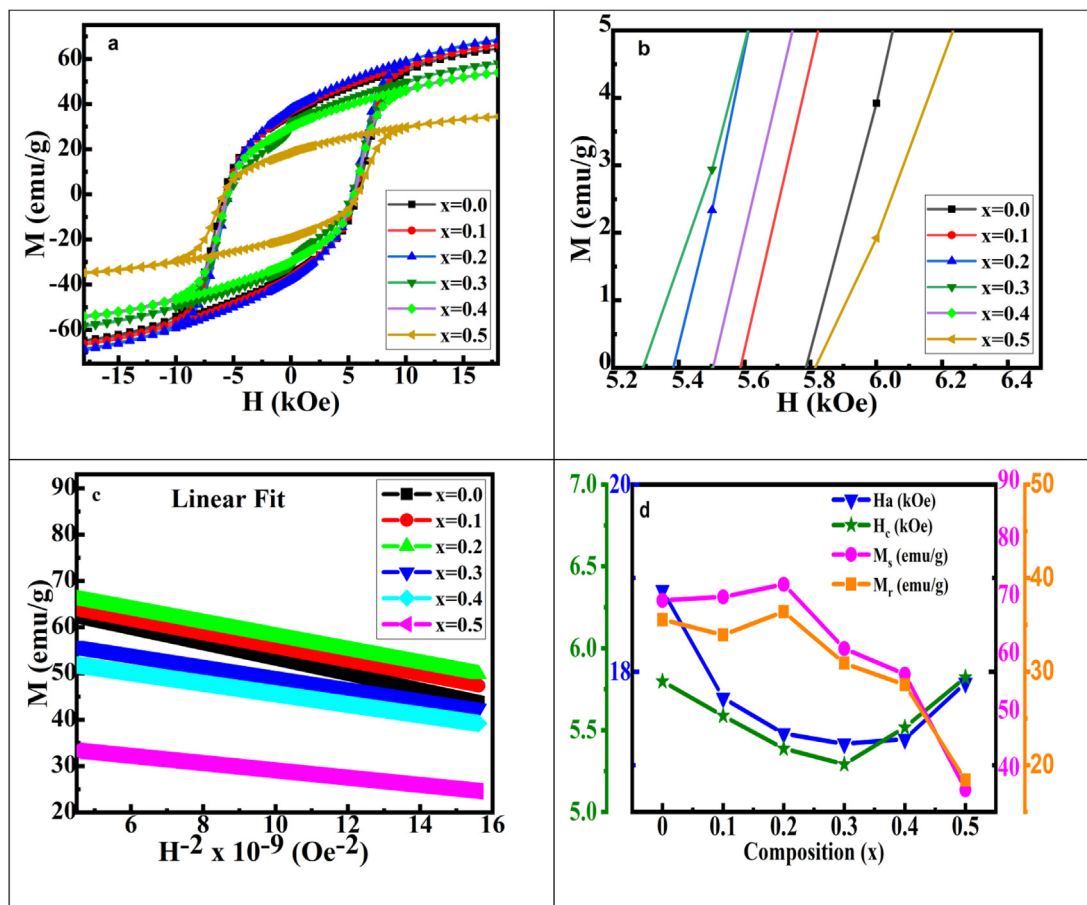
**Fig. 6.** Magnetic measurement of $Sr_{(1-x)}Ca_xFe_{12}O_{19}$ (x = 0.0–0.5) samples: a) M vs. H graphs, b) zoomed view of M vs. H graphs, c) linear fitting of M vs. $1/H^2$ to determine $M_s$ and d) graphs of $H_a$, $M_s$, $M_r$ and $H_c$ vs. composition.

**Table 3**
Magnetic parameters for $Sr_{(1-x)}Ca_xFe_{12}O_{19}$ (x = 0.0–0.5) samples.

| Composition (x) | $H_c$ (Oe) | $M_s$ (emu/g) | $M_r$ (emu/g) | $M_r/M_s$ | Ha (kOe) |
|---|---|---|---|---|---|
| 0.0 | 5799 | 35.55 | 69.83 | 0.5090 | 18.87 |
| 0.1 | 5588 | 33.95 | 70.45 | 0.5102 | 17.72 |
| 0.2 | 5388 | 36.42 | 72.63 | 0.5014 | 17.34 |
| 0.3 | 5292 | 30.91 | 61.48 | 0.5027 | 17.23 |
| 0.4 | 5517 | 28.61 | 57.01 | 0.5018 | 17.28 |
| 0.5 | 5823 | 18.42 | 36.89 | 0.4993 | 17.88 |

## Declaration of Competing Interest

The authors declare that they have no known competing financial interests or personal relationships that could have appeared to influence the work reported in this paper.

## Acknowledgments

## References

Blanco, A.M., Gonzalez, F.C., 1989. Magnetic properties and phase equilibrium in the BaO-CaO-Fe$_2$O$_3$ system. J. Phys. D Appl. Phys. 22 (1), 210–215.

Mehtab, A., Ahmed, J., Alshehri, S.M., Mao, Y., Ahmad, T., 2022. Rare earth doped metal oxide nanoparticles for photocatalysis: a perspective. Nanotechnol. 33,. https://doi.org/10.1088/1361-6528/ac43e7 142001.

Ashima, Sanghi, S., Agarwal, A., Reetu, 2012. Rietveld refinement, electrical properties and magnetic characteristics of Ca-Sr substituted barium hexaferrites. J. Alloys Compd. 513, 436–444. https://doi.org/10.1016/j.jallcom.2011.10.071.

Hooda, A., Sanghi, S., Agarwal, A., Dahiya, R., 2015. Crystal structure refinement, dielectric and magnetic properties of Ca/Pb substituted SrFe$_{12}$O$_{19}$ hexaferrites. J. Magn. Magn. Mater. 387, 46–52. https://doi.org/10.1016/j.jmmm.2015.03.078.

Shirk, B.T., Buessem, W.R., 1970. Magnetic properties of barium ferrite formed by crystallization of a glass. J. Am. Ceram. Soc. 53, 192–196. https://doi.org/10.1111/j.1151-2916.1970.tb12069.x.

Chauhan, C.C., Kagdi, A.R., Jotania, R.B., Upadhyay, A., Sandhu, C.S., Shirsath, S.E., Meena, S.S., 2018. Structural, magnetic and dielectric properties of Co-Zr substituted M-type calcium hexagonal ferrite nanoparticles in the presence of $\alpha$-Fe$_2$O$_3$ phase. Ceram. Int. 44 (15), 17812–17823. https://doi.org/10.1016/j.ceramint.2018.06.249.

Singh, C, Bindra Narang, S., Hudiara, I.S., Bai, Y., Tabatabaei, F., 2008. Static magnetic properties of Co and Ru substituted Ba – Sr ferrite. Mater. Res. Bull. 43 (1), 176–184. https://doi.org/10.1016/j.materresbull.2007.06.050.

Lotgering, F.K., Huyberts, M.A.H., 1980. Composition and magnetic properties of hexagonal Ca, La ferrite with magnetoplumbite structure. Solid State Commun. 34 (1), 49–50. https://doi.org/10.1016/0038-1098(80)90627-4.

Ali, I., Islam, M.U., Awan, M.S., Ahmad, M., Asif Iqbal, M., 2013. Structural, electrical, and microstructure properties of nanostructured calcium doped Ba-Hexaferrites synthesized by Sol-Gel method. J. Supercond. Nov. Magn. 26 (11), 3277–3286. https://doi.org/10.1007/s10948-013-2167-7.

Musa, I.M., Abdu, Y., Mohammed, J., Srivastava, A.K., 2021. Structural, dielectric and Raman spectroscopy of La$^{3+}$–Ni$^{2+}$–Zn$^{2+}$ substituted M-type strontium hexaferrites. Cryst. Res. Technol. 2100005. https://doi.org/10.1002/crat.202100005.

Mohammed, J., Suleiman, A.B., Hafeez, H.Y., Carol T, T.T., Sharma, J., Bhadu, G.R., Kumar Godara, S., Srivastava, A.K., 2018a. Effect of heat-treatment on the magnetic and optical properties of Sr$_{0.7}$Al$_{0.3}$Fe$_{11.4}$Mn$_{0.6}$O$_{19}$. Mater. Res. Exp. 5 (8), 086106. https://doi.org/10.1088/2053-1591/aad1e5.

Mohammed, J., Sharma, J., Yerima, K.U., Carol, T.T.T., Basandrai, D., Kumar, A., Maji, P.K., Srivastava, A.K., 2020. Magnetic, Mössbauer and Raman spectroscopy of nanocrystalline Dy$^{3+}$-Cr$^{3+}$ substituted barium hexagonal ferrites. Phys. B: Condens. Matter. 585,. https://doi.org/10.1016/j.physb.2020.412115 412115.

Mohammed, J., Hafeez, H.Y., Trudel, T.T.C., Ndikilar, C.E., Sharma, J., Maji, P.K., Godara, S.K., Srivastava, A.K., 2019. Structural, dielectric, and magneto-optical properties of Cu$^{2+}$- Er$^{3+}$ substituted nanocrystalline strontium hexaferrite. Mater. Res. Exp. 6,. https://doi.org/10.1088/2053-1591/ab063b 056111.

Mohammed, J., Suleiman, A.B., Tchouank Tekou Carol, T., Hafeez, H.Y., Sharma, J., Maji, P.K., Kumar, S.G., Srivastava, A.K., 2018b. Enhanced dielectric and optical properties of nanoscale barium hexaferrites for optoelectronics and high frequency application. Chinese Phys. B 27 (12), 128104. https://doi.org/10.1088/1674-1056/27/12/128104.

Christy, J.N., Rewatkar, K.G., Sawadh, P.S., 2019. Structural and dielectric properties of substituted calcium hexaferrites. Int. J. Eng. Res. Technol. 8, 178–182 https://www.ijert.org/structural-and-dielectric-properties-of-substituted-calcium-hexaferrites.

Habanjar, K., Shehabi, H., Abdallah, A.M., Awad, R., 2020. Effect of calcination temperature and cobalt addition on structural, optical and magnetic properties of barium hexaferrite BaFe$_{12}$O$_{19}$ nanoparticles. Appl. Phys. A Mater. Sci. Process. 126, 402. https://doi.org/10.1007/s00339-020-03497-3.

Yuping, L., Daxin, B., Zhangzhong, W., Zhang, Y., Lizhao, C., Guangcheng, Z., Mengling, W., 2018. Fabrication of M-type ferrites with high La-Co concentration through Ca$^{2+}$ doping. J. Alloys Compd. 734, 130–135. https://doi.org/10.1016/j.jallcom.2017.11.050.

Urbano-Peña, M.A., Palomares-Sánchez, S.A., Betancourt, I., Pérez-Juache, T.J., Ruiz, F., 2019. Effect of temperature on the magnetic properties of strontium hexaferr0000ite synthesized by the Pechini method. Appl. Phys. A Mater. Sci. Process. 125, 711. https://doi.org/10.1007/s00339-019-3004-z.

Ubaidullah, M., Ahmed, J., Al-Enizi, A.M., Tyagi, A., Shaikh, S.F., Tarannum, N., Ahmad, T., 2020. Metal organic precursor derived Ba1-xCaxZrO3 (0.05 ≤ x ≤ 0.20) nanoceramics for excellent capacitor applications. J. King Saud Univ. Sci. 32 (3), 1937–1943. https://doi.org/10.1016/j.jksus.2020.02.009.

Alhokbany, N., Almotairi, S., Ahmed, J., Al-Saeedi, S.I., Ahamad, T., Alshehri, S.M., 2021. Investigation of structural and electrical properties of synthesized Sr-doped lanthanum cobaltite (La$_{1-x}$Sr$_x$CoO$_3$) perovskite oxide. J. king Saud Uni. Sci. 33 (4), 101419. https://doi.org/10.1016/j.jksus.2021.101419.

Pullar, R.C., 2012. Hexagonal ferrites: a review of the synthesis, properties and applications of hexaferrite ceramics. Prog. Mater. Sci. 57 (7), 1191–1334. https://doi.org/10.1016/j.pmatsci.2012.04.001.

Jasrotia, R., Singh, V.P., Kumar, R., Singh, M., 2020. Raman spectra of sol-gel auto-combustion synthesized Mg-Ag-Mn and BaNd-Cd-In ferrite based nanomaterial. Ceram. Int. 46, 618–621. https://doi.org/10.1016/j.ceramint.2019.09.012.

Kumar, S., Supriya, S., Pandey, R., Pradhan, L.K., Singh, R.K., Kar, M., 2018. Effect of lattice strain on structural and magnetic properties of Ca substituted barium hexaferrite. J. Magn. Magn. Mater. 458, 30–38. https://doi.org/10.1016/j.jmmm.2018.02.093.

Kumar, S., Kaur, T., Kumar, S., Srivastava, A.K., 2015. Effect of heat treatment on properties of Sr$_{0.7}$Nd$_{0.3}$Co$_{0.3}$Fe$_{11.7}$O$_{19}$. J. Supercond. Nov. Magn. 28 (10), 2935–2940. https://doi.org/10.1007/s10948-015-3105-7.

Godara, S.K., Singh, M., Kaur, V., Narang, S.B., Chaudhari, J.C., Bhadu, G.R., Mudsainiyan, R.K., Sood, A.K., 2019. Tunable M-type nano barium hexaferrites material by Zn$^{2+}$/Zr$^{4+}$ co-doping. Mater. Res. Express. 6, (2019) 116111.

Godara, S.K., Singh, M., Kaur, V., Narang, S.B., Sood, A.K., 2021a. Effect of calcium solubility on structural, microstructural and magnetic properties of M-type barium hexaferrite. Ceram. Int. 47 (14), 20399–20406. https://doi.org/10.1016/j.ceramint.2021.04.048.

Godara, S.K., Singh, M., Kaur, V., Narang, S.B., Ahmed, J., Sood, A.K., 2022. Effect of calcium solubility on structural, microstructure and magnetic properties of SrFe$_{12}$O$_{19}$. Phys. B: Condens. Matter 628, 413560. https://doi.org/10.1016/j.physb.2021.413560.

Godara, S.K., Kaur, V., Chuchra, K., Narang, S.B., Singh, G., singh, M., chawla, A., Verma, S., Bhadu, G.R., Chaudhari, J.C., Babu, P.D., Sood, A.K., 2021b. Impact of Zn$^{2+}$-Zr$^{4+}$ substitution on M-type barium strontium hexaferrite's structural, surface morphology, dielectric and magnetic properties. Results Phys. 22, 103892. https://doi.org/10.1016/j.rinp.2021.103892.

Sable, S.N., Rewatkar, K.G., Nanoti, V.M., 2010. Structural and magnetic behavioral improvisation of nanocalcium hexaferrites. Mater. Sci. Eng. B Solid-State Mater. Adv. Technol. 168 (1-3), 156–160. https://doi.org/10.1016/j.mseb.2009.10.034.

Ahmad, T., Khatoon, S., Coolahan, K., Lofland, S.E., 2013. Solvothermal synthesis, optical and magnetic properties of nanocrystalline Cd$_{1-x}$Mn$_x$O (0.04 < $x$ = 0.10) solid solutions. J. Alloys Compd. 558, 117–124. https://doi.org/10.1016/j.jallcom.2012.12.159.

Kaur, T., Sharma, J., Kumar, S., Srivastava, A.K., 2017. Optical and multiferroic properties of Gd-Co substituted barium hexaferrite. Cryst. Res. Technol. 52 (9), 1700098. https://doi.org/10.1002/crat.201700098.

Trudel, T.T.C., Mohammed, J., Hafeez, H.Y., Bhat, B.H., Godara, S.K., Srivastava, A.K., 2019. Structural, dielectric, and magneto-optical properties of Al-Cr substituted M-type barium hexaferrite. 216 (26), 1800928. doi: 10.1002/pssa.201800928.

Yang, Y., Liu, X., Jin, D., Ma, Y., 2014. Structural and magnetic properties of La-Co substituted Sr-Ca hexaferrites synthesized by the solid state reaction method. Mater. Res. Bull. 59, 37–41. https://doi.org/10.1016/j.materresbull.2014.06.003.

Li, Z.W., Ong, C.K., Yang, Z., Yang, Z., Wei, F.L., Zhou, X.Z., Zhao, J.H., Morrish, A.H., 2000. Site preference and magnetic properties for a perpendicular recording material: BaFe$_{12-x}$Zn$_{x/2}$Zr$_{x/2}$O$_{19}$ nanoparticles. Phys. Rev. B – Condens. Matter Mater. Phys. 62, 6530–6537. https://doi.org/10.1103/PhysRevB.62.6530.